Check for updates

Advanced Energy Materials

WILEY | ADVANCED ENERGY MATERIALS
www.advenergymat.de

RESEARCH ARTICLE OPEN ACCESS

Dendrite Formation and Self-Healing Mechanism in Ionic Liquid-Based Magnesium Batteries

Omar W. Elkhafif[1] | Yuanzhu Zhao[2] | Zhenyu Guo[2] | Maria-Magdalena Titirici[2,3] | Timo Jacob[1,4,5] | Hagar K. Hassan[1,4,5]

[1]Institute of Electrochemistry, Ulm University, Ulm, Germany | [2]Department of Chemical Engineering, Imperial College London, London, UK | [3]Advanced Institute for Materials Research (WPI-AIMR), Tohoku University, Sendai, Miyagi, Japan | [4]Department of Electrochemistry II and Theory I, Helmholtz-Institute-Ulm (HIU), Ulm, Germany | [5]Karlsruhe Institute of Technology (KIT), Karlsruhe, Germany

Correspondence: Timo Jacob (timo.jacob@uni-ulm.de) | Hagar K. Hassan (hagar.khalil-hassan@uni-ulm.de)

Received: 20 September 2025 | **Revised:** 10 November 2025 | **Accepted:** 12 November 2025

Keywords: dendrites | ionic liquids | rechargeable Mg batteries | self-healing | self-heating

ABSTRACT

Magnesium (Mg) is set as a viable alternative battery material to lithium (Li) owing to its cost, natural abundance, and safety. Nevertheless, the formation of dendrites on Mg anodes remains controversial. While some studies refute their existence, others report contradictory findings influenced by current density and the insufficiently understood roles of electrolyte formulation, additives, and temperature. In this work, these parameters are systematically investigated using symmetric Mg|Mg and asymmetric Mg|TiS_2 cells with tailored ionic-liquid-based electrolytes. Furthermore, *operando* optical microscopy is employed to visualize nucleation and dendritic growth at different current densities. At low current densities (0.1–0.5 mA cm^{-2}), non-uniform island-like Mg deposits evolved into soft dendrites, finally leading to short-circuiting. Contrary, higher current densities (1–5 mA cm^{-2}) promote uniform, spherical deposits and facilitate stable cycling over 700 cycles. In Mg|TiS_2 asymmetric cells, enhanced cycling stability is observed at 50 mA g^{-1}, whereas soft dendrite formation at 10 mA g^{-1} leads to cell failure within 30 cycles. Taking advantage of Mg's safety, cycling of symmetric cells are continued even beyond dendrite-forming to study morphological and mechanical recovery. Notably, our analysis reveales self-healing due to dendrite fusion in previously short-circuited cells. These findings reveal conditions affecting Mg dendrite behavior, highlighting the key roles of current density and temperature in developing stable, rechargeable Mg batteries, and reporting self-healing in Mg batteries for the first time.

1 | Introduction

Rechargeable magnesium batteries (RMBs) have gained considerable attention as one of the promising candidates to replace lithium-ion batteries. This is primarily owing to their merit properties, including bivalency of Mg^{2+} ions, abundant availability, and substantial volumetric capacity by a factor of 1.8 times compared to Li metal [1–3]. One of the main challenges of Li-metal batteries is the formation of sharp dendrites during cycling, which can lead to short circuits and thermal runaway, posing serious risks of fire or explosion [4]. It was previously believed that Mg batteries are dendrite-free, making them safer than their lithium counterparts [5–10]. However, recent studies have shown that Mg electrodes can indeed form dendrites [11–16]. The main cause for dendrite formation in RMBs is still uncertain, and different causal factors have been reported. One of the main reasons is the irregularity and irreversibility of Mg deposition and stripping. For instance, the non-uniform Mg dissolution leads to degradation of the Mg anode and consequently to dendrite formation [11, 17]. The trigger for irreversible Mg deposition/stripping is the high Mg reactivity that undergoes a passivation reaction in most of the known electrolytes [11, 18, 19]. Furthermore, electrolyte

This is an open access article under the terms of the Creative Commons Attribution License, which permits use, distribution and reproduction in any medium, provided the original work is properly cited.

© 2025 The Author(s). Advanced Energy Materials published by Wiley-VCH GmbH

decomposition as well as trace amounts of water are key factors for Mg surface passivation [20, 21]. Such a phenomenon reduces the active sites on the Mg electrode surface and results in high local current densities [11, 22]. Another significant factor is the applied current density; however, the relationship between the applied current density and dendrite formation is debatable, with a considerable degree of discrepancies reported in the literature. A few studies report that Mg dendrite formation accelerates at relatively high current densities ($\geq$ 5 mA cm^{-2}), with current density strongly influencing dendrite morphology, for instance, mossy-like structures at 5 mA cm^{-2} versus interconnected islands at 10 mA cm^{-2} [13, 15]. However, other reports have detected Mg dendrites at current densities below the previously mentioned value, likely due to irreversible Mg deposition and stripping reactions. This results in a rougher and more intricate structure, resembling dendrite growth in Li batteries [11, 14, 17, 23]. To address this issue, various strategies have been proposed to suppress or prevent dendrite formation in Mg metal batteries. Modification of the Mg anode by introducing an artificial solid electrolyte interface (SEI) was proposed to avoid passivation of the Mg electrode [24]. Here, the formation of an ionically conducting and electronically insulating MgF_2 layer on the Mg electrode surface improved its voltage stability, cyclic performance, as well as coulombic efficiency [24]. Furthermore, introducing magnesiophilic sites on the Mg anode has been found to inhibit needle-like Mg dendrites and promote spherical Mg deposition even at very high current densities [13, 25]. This has been achieved by coating with Au nanoseeds, leading to a thermodynamically spontaneous reaction and the formation of a Mg–Au alloy [13]. On the other hand, the introduction of 1-chloropropane to the $Mg(OTF)_2$/DME system enhanced the planar Mg deposition associated with the formation of a protective interphase [26].

While many studies have focused on Mg dendrite formation or current density effects, overlooking cycle number, electrolyte composition, additives (chloride-free vs. chloride-containing), and operating temperature must be addressed. Safety concerns and thermal runaway were entirely ignored. Thus, due to limited understanding of Mg dendrite growth parameters, we investigated factors influencing dendrite formation and short-circuiting in Mg|Mg symmetric cells using our optimized MIDS electrolyte, 0.1 M $Mg(TFSI)_2$ + 0.01 M $Mg(BH_4)_2$ in (1:3) MPPip-TFSI: diglyme, by utilizing galvanostatic cyclic and electrochemical impedance spectroscopy (EIS). Different factors affecting the Mg growth mechanism, including current density, electrolyte additives, and measurement temperature, were studied. Scanning electron microscopy (SEM) with energy dispersive X-ray spectroscopy (EDS) was utilized to visualize the formation and suppression of dendrites upon cycling. Interestingly, upon cycling, the short-circuited cell did not exhibit any thermal runaway; rather, a cell recovery was observed, followed by a long-range cycling stability. Moreover, a layered TiS_2 was utilized in this study as a proof-of-concept since it has been widely explored in Mg batteries [27–30], due to the improved Mg mobility in sulfide structures compared to the sluggish diffusion in oxides [27]. It is found that achieving a high performance and long-term stability is highly dependent on the water content inside the cathode material and the current density. An improved cycling stability was achieved at a relatively high specific current of 50 mA g^{-1}, while soft dendrites were observed at a lower specific current of 10 mA g^{-1}. At room temperature, and without prior modification of TiS_2 prepared inside the glovebox, a maximum capacity of 200 mAh g^{-1} was achieved.

2 | Results and Discussion

2.1 | Mg Dendrite Formation in MIDS Electrolytes

Since the applied current is a crucial factor for electrolyte stability and the formation of the solid–electrolyte interphase (SEI), an initial investigation was conducted to gain detailed insights into its impact. Galvanostatic measurements at different currents were performed to study the voltage profile. During galvanostatic cycling, in situ EIS was recorded every 20 cycles to track SEI evolution as well as possible surface changes since it is one of the most straightforward, sensitive, and highly informative analytical methods [31]. Figure 1a illustrates galvanostatic cycling profiles accompanied by EIS in a Mg|Mg symmetric cell at applied currents of 0.01, 0.025, 0.05, 0.1, 0.15, 0.2, 0.4, and 0.5 mA cm^{-2}, consecutively. For each current from 0.01 to 0.4 mA cm^{-2}, 20 cycles were conducted, and the voltage profile was analysed. For currents from 0.01 to 0.2 mA cm^{-2}, a nearly constant voltage profile can be observed, with Mg depositing at −0.3 V and dissolving at 0.3 V vs. $Mg|Mg^{2+}$, as shown in Figure 1b. However, upon doubling the current from 0.2 to 0.4 mA cm^{-2}, a higher overpotential was observed; thus, the voltage profile increased to a range from −0.6 to 0.6 V. After a few cycles, a short circuit occurred with an overpotential between −0.005 and 0.005 V vs. $Mg|Mg^{2+}$ [32]. At this point, EIS showed a small semicircle with a very low resistance of 12 Ω compared to a total impedance of approximately 6000 Ω at open-circuit voltage (OCV), as shown in Figure 1c, indicating dendrite formation. Hard short circuits create a permanent electronic path with resistance similar to that of a metal wire (electron transport). In contrast, soft short circuits resulting from small localized electronic connections between the working and counter electrodes enable both direct electron transfer and interfacial electrochemical reactions (electronic and ionic) [33, 34]. The absence of a single-point EIS response, typical of hard dendrites, indicates soft dendrites are more likely.

This phenomenon suggests that either the increase in applied current is responsible for dendrite formation and the subsequent short circuit, as reported in Ref. [35], or long-term cycling is the primary cause, which will be investigated later. Figure 1d shows optical images of the WE, CE, and GF separator of a cell that was stopped at the short circuit. It is clearly shown that dendrites had formed at a small, localized spot, which is in agreement with previous reports [11, 14]. The actual current density in this case is questionable due to partial surface passivation or non-uniform deposition, resulting in a highly inhomogeneous current density distribution. Given the fact that Mg is safer than Li in terms of thermal runaway, cycling of the short-circuited cell was continued at 0.1 mA cm^{-2}. After approximately 25 cycles, voltage plateaus at −1.2 and 0.6 V vs. $Mg|Mg^{2+}$ were observed, which stabilized at −0.4 and 0.4 V vs. $Mg|Mg^{2+}$ after a few additional cycles for approximately 50 cycles, indicating unexpected cell recovery.

Subsequently, enhanced performance was observed in the consecutive cycles, with voltage plateaus at −0.2 and 0.2 V vs. $Mg|Mg^{2+}$. The current was then increased fivefold in order to

16146840, 0, Downloaded from https://advanced.onlinelibrary.wiley.com/doi/10.1002/aenm.202505315 by Karlsruher Institut Für Technologie, Wiley Online Library on [04/12/2025]. See the Terms and Conditions (https://onlinelibrary.wiley.com/terms-and-conditions) on Wiley Online Library for rules of use; OA articles are governed by the applicable Creative Commons License

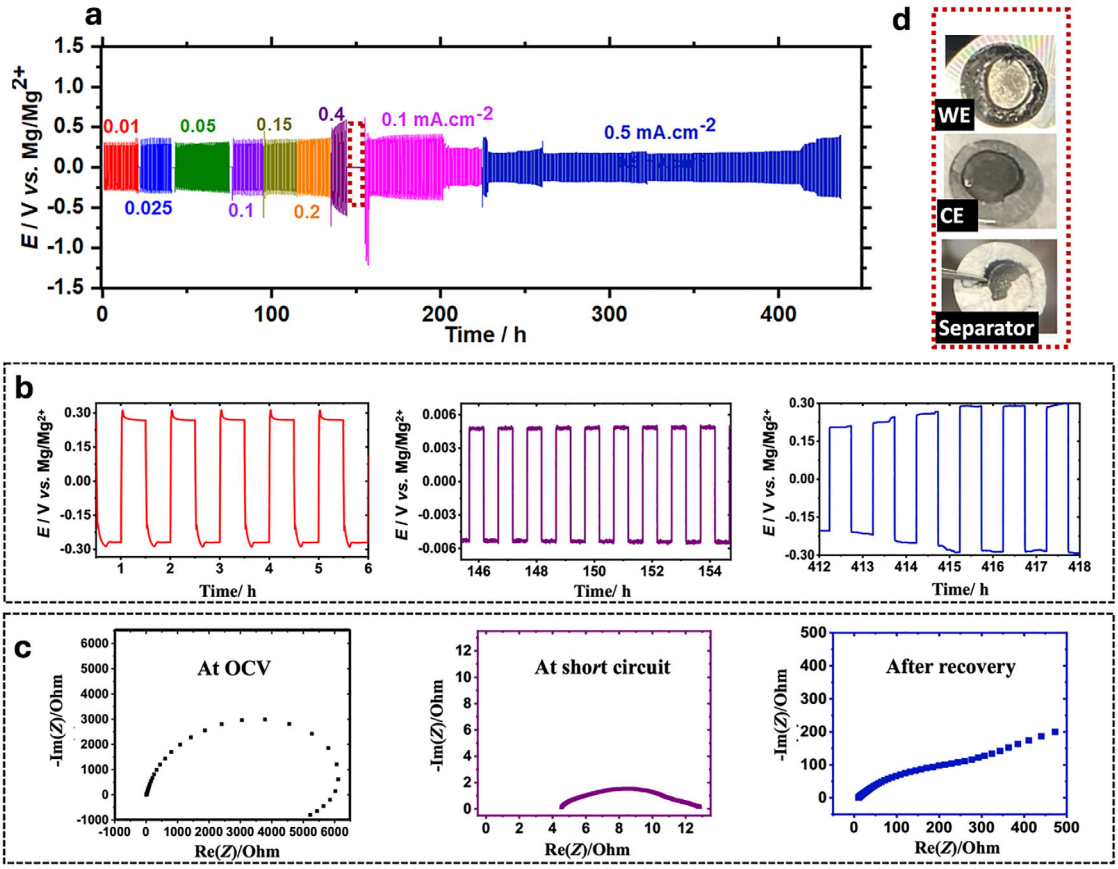

FIGURE 1 | (a) Galvanostatic cycling of a symmetric Mg cell in the MIDS electrolyte at different currents of 0.01, 0.025, 0.05, 0.1, 0.15, 0.2, 0.4, 0.5 mA cm^{-2} tested in a BOLA cell; (b) Voltage profiles for the first six cycles, at short circuit (cycle 146 to 154), and after recovery (cycle 412 to 418); (c) Nyquist plots of the Mg|Mg cell at OCV, at the short circuit and after 450 cycles (i.e., after recovery), respectively; (d) Optical images of the working electrode (WE), counter electrode (CE) and glass fibre (GF) separator of the dendritic cell (at short circuit).

investigate the potential reformation of dendrites; however, this did not occur, and enhanced cyclability was observed instead. As shown in Figure 1b, voltage plateaus at −0.2 and 0.2 V vs. $Mg|Mg^{2+}$ were maintained for over 200 cycles, slightly increasing to −0.3 and 0.3 V vs. $Mg|Mg^{2+}$, which are identical to the overpotentials observed during the initial cycles. The Nyquist plot after 450 cycles, shown in Figure 1c left, reveals Warburg impedance, indicating a diffusion-controlled process with relatively lower impedance compared to before cycling. The retention of cell impedance and galvanostatic cycling performance, including deposition/ stripping overpotentials, provides strong evidence for cell healing after a short circuit.

Furthermore, to investigate whether or not the higher current density or the repeated cyclability is the primary reason for dendrite formation, a new investigation was conducted using galvanostatic cycling for symmetric Mg|Mg cells operated for up to 500 cycles at 0.1 mA cm^{-2} as shown in Figure 2a. SEM, and *operando* EIS were used to reveal the microstructure evolution of Mg deposits during cycling, at and after dendrite formation, and after cell recovery. As shown in Figure 2b, the Nyquist plot of the symmetric cell at OCV revealed a semicircle indicating a charge transfer resistance related to a diffusion-limited process or sluggish reaction kinetics [36]. While the SEM micrograph of the pristine Mg electrode at OCV exhibited a rough plain surface due to the mechanical polishing of the surface, removing the thin oxide layer, as shown in Figure 2c. After 50 cycles, the Nyquist plot exhibited a semicircle in the high-frequency region and a diffusion tail in the low-frequency region with a lower overall impedance compared to the initial EIS, indicating the formation of the SEI layer (Figure 2d). At this point, the SEM micrograph showed a fine and uniform deposition of Mg over the surface of the electrode as observed in Figure 2e. After 140 cycles, a very low voltage profile was observed with a cell impedance of 30 Ω, as observed in Figure 2f, indicating the formation of soft dendrites. At the short circuit, the dendritic electrode showed dense mossy-like structures as shown in Figure 2g, rather than the typical needle- or filament-like structures characteristic of hard dendrites [37–39]. This is in contrast to the interconnected spherical deposits with lamellae substructure that were reported previously by Ding et al. and Ha et al [11, 40]. This difference in morphology is attributed to changes in the electrolyte composition as reported in our previous work [41]. Further cycling resulted in cell healing, where the Nyquist plot (Figure 2h), as well as the voltage profiles were partially recovered but showed some fluctuations and instabilities for approximately 100 cycles, as shown in Figure 2a. The SEM micrograph of the electrode at this stage showed a less dense and relatively smooth surface, as shown in Figure 2i. No further dendrites formed for up to 500 cycles; instead, the galvanostatic cycling stabilized, as clearly shown in Figure 2a. The Nyquist plot at the end of cycling (Figure 2j) displayed a diffusion tail forming a 45° angle with the

16146840, 0, Downloaded from https://advanced.onlinelibrary.wiley.com/doi/10.1002/aenm.202505315 by Karlsruher Institut Für Technologie, Wiley Online Library on [04/12/2025]. See the Terms and Conditions (https://onlinelibrary.wiley.com/terms-and-conditions) on Wiley Online Library for rules of use; OA articles are governed by the applicable Creative Commons License

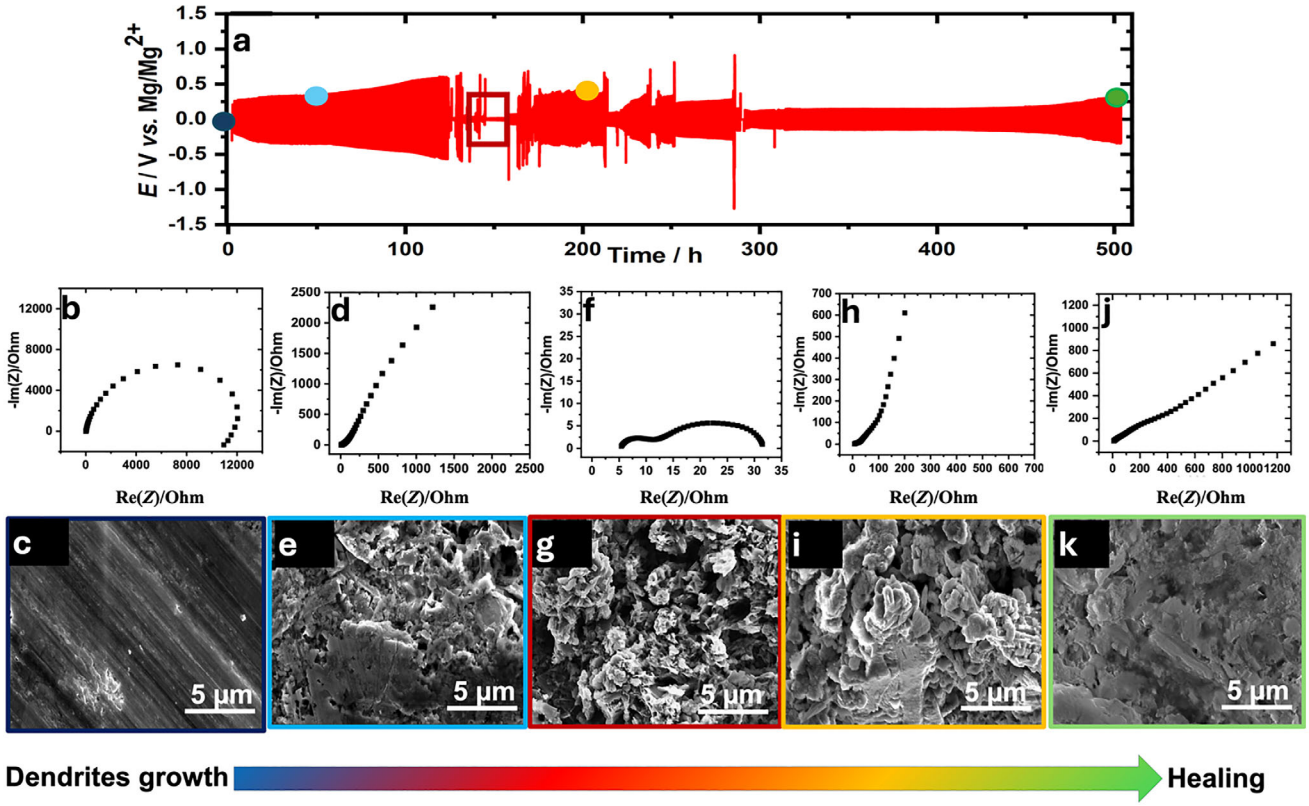

FIGURE 2 | (a) Galvanostatic cycling of a symmetric Mg cell in the MIDS electrolyte at 0.1 mA cm^{-2}, (b) Nyquist plots of the pristine Mg electrode at OCV, (c) SEM micrographs of Mg electrode at OCV, (d) Nyquist plot after 50 cycles, (e) The corresponding SEM micrographs of Mg electrode after 50 cycles (f) Nyquist plot at the short circuit, (g) The corresponding SEM micrographs of the Mg electrode at short circuit (h) Nyquist plot after 50 cycles from cell healing, (i) The corresponding SEM micrographs of Mg electrode after 50 cycles from self-healing, (j) Nyquist plot at the end of cycling, and (k) The corresponding SEM micrograph of Mg electrode at the end of cycling. The measurements were taken from four different cells that were tested under the same conditions but stopped at different cycling stages for SEM imaging.

x-axis, revealing a diffusion-controlled process and confirming cell recovery, while a highly smooth dendrite-free surface could be observed by SEM (Figure 2k).

Since dendrite formation is a fatal issue, understanding its growth kinetics is crucial. Metal dendrites usually tend to nucleate and grow during electrochemical cycling, manifested in a low columbic efficiency [37]. Parasitic side reactions, irreversible capacity loss at the anode, and continuous growth of the SEI layer also result in dendrite growth [37]. Previous reports claimed that high current densities (5–20 mA cm^{-2}) as well as a high surface reactivity of magnesium trigger passivation layer formation [13, 42].

Although this layer suppresses surface reactions, it simultaneously hinders Mg^{2+} ion transport and self-diffusion. Due to its inhomogeneous distribution, this passivation process promotes non-uniform Mg deposition and dendrite formation [12–15, 43]. On the contrary, a discrepancy has been noticed for the role of the current density. For instance, other reports claimed dendrite formation already at relatively low current densities [4, 12, 14, 44–46]. Furthermore, the influence of deposition potential on the morphology of the deposited Mg was found to be highly dependent on the nature of the surface [12]. For instance, the Mg(0001) surface showed very weak potential dependency that did not influence the formation of packed morphologies on the surface [12, 47]. Several other reports proposed that the diffusion barrier is a good descriptor for dendrite growth [43, 48–50]. However, theoretical calculations revealed that the diffusion barrier on the most prevalent Mg surface under standard operating conditions is sixfold higher than that on Li electrodes. As the terrace self-diffusion of an atom is almost zero on Mg(0001), while with a higher activation energy on Mg(10$\bar{1}$1)) Those findings point out that Mg could be more susceptible to dendrite formation than Li [12, 47]. Consequently, diffusion barriers are insufficient to describe dendrite growth [12]. Ding et al. attributed dendrite formation to the spontaneous decomposition of $TFSI^-$ anions on freshly deposited Mg in the electrolyte, which has a pronounced tendency to decompose upon cycling, triggering the formation of MgF_2 and MgS that passivate deposited Mg. Upon cycling, these interconnected passivated islands form dendrites that grow toward the other electrode, causing a short circuit [11]. However, in another study by Li et al., MgF_2 was reported as an artificial interphase that successfully prevented soft dendrite formation and protected the Mg anode [24]. The high porosity, electronic insulating properties, and high ionic conductivity of MgF_2 facilitated Mg^{2+} diffusion to bulk Mg, enabling interactions beneath the protective film [24]. Thus, the primary cause of dendrite formation remains uncertain, and further fundamental investigations are required.

16146840, 0, Downloaded from https://advanced.onlinelibrary.wiley.com/doi/10.1002/aenm.202505315 by Karlsruher Institut Für Technologie, Wiley Online Library on [04/12/2025]. See the Terms and Conditions (https://onlinelibrary.wiley.com/terms-and-conditions) on Wiley Online Library for rules of use; OA articles are governed by the applicable Creative Commons License

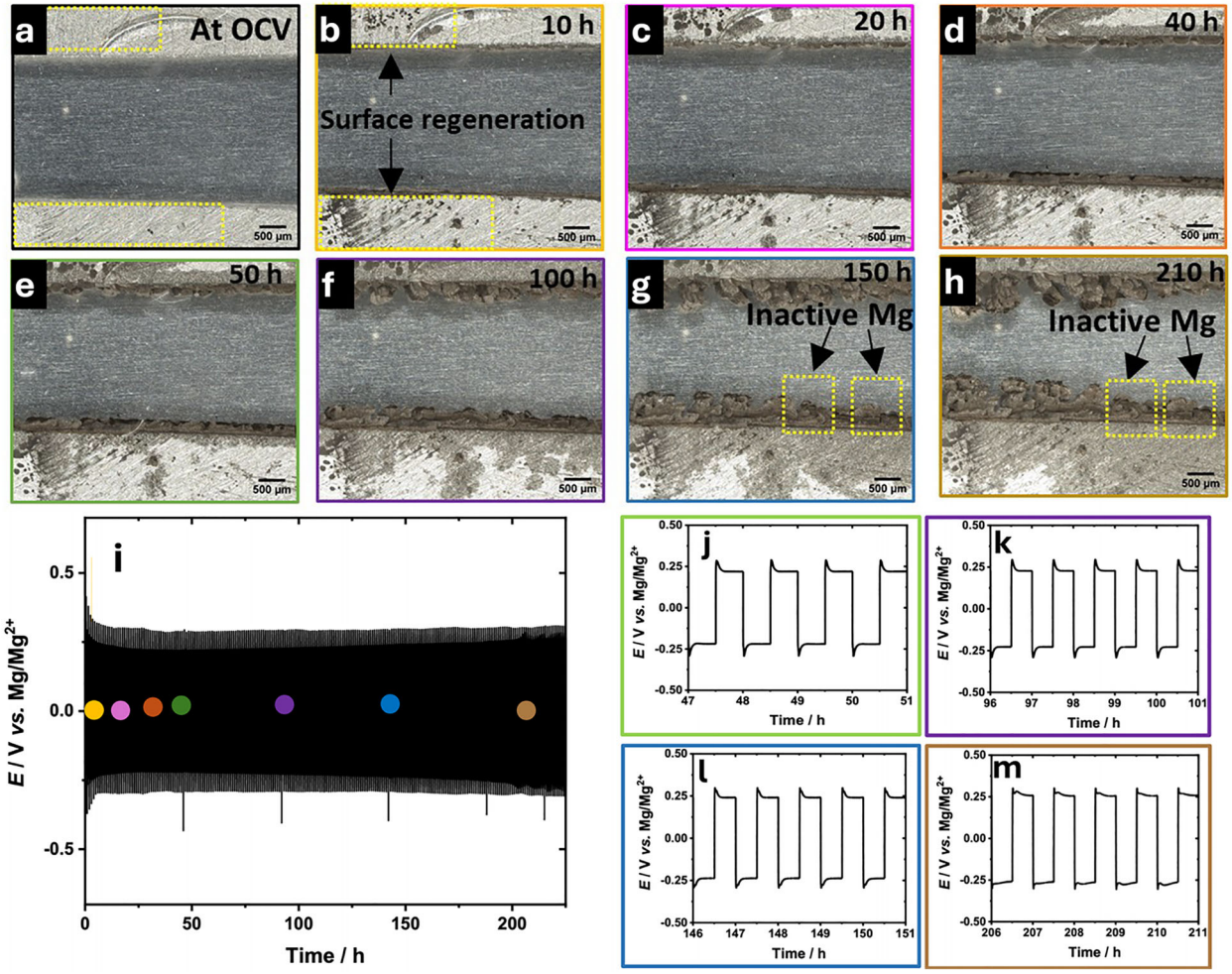

FIGURE 3 | (a–h) *Operando* optical microscopy images for the Mg|Mg cell operating with an apparent current density of 0.12 mA cm^{-2}recorded at different times in a corresponding electrochemical cell. On each image, the exact time is indicated, as well as yellow dotted rectangles that highlight surface regeneration and inactive Mg. (i) Galvanostatic cycling of the symmetric Mg cell, where the color of each point indicates the corresponding image, (j–m) zoomed-in galvanostatic cycling to show the voltage profiles of the cell after 50, 100, 150, 200 cycles.

To gain deeper insights into the formation of dendrites and cell recovery after a short circuit, *operando* optical microscopy was utilized to visualize morphological changes. Thanks to the stability of our MIDS electrolyte, it was possible to record images for more than 500 h of operation at a current of 0.102 mA. Optical images of the Pouch cell electrodes as well as the full galvanostatic cycling are illustrated in Figure S1 and Figure S2, respectively. Visualization of the cell operation presented important insights into the Mg growth and its morphology at different stages, as illustrated in Figure 3a–h. During preparation of the Mg electrodes, only edges were sanded and polished to remove the oxide layer and facilitate activation. However, after the initial cycling process, the upper surface of the electrodes gradually became activated and exhibited increased conductivity, as observed after 10 h of cycling (Figure 3b). The high reducing property of $Mg(BH_4)_2$ has a vital and crucial role in the surface activation as it interacts with the electrode surface by removing the passivating oxide layer [51, 52]. However, this resulted in changes in the applied current densities. Meanwhile, a non-uniform Mg deposition was observed already from the early cycles, as shown in Figure 3a–f. It could also be observed that Mg prefers to deposit on freshly deposited clusters instead of initiating additional nucleation centers, resulting in a vertical growth of Mg dendrites. It is also noticed that some spots stopped growing, indicating the formation of inactive Mg (yellow marked in Figure 3g,h) that are electronically disconnected from the conductive Mg surface. One of the reasons for the formation of this inactive Mg could be the spontaneous adsorption and decomposition of $TFSI^-$ anions on the surface of freshly deposited Mg into electronically insulating products [11, 24]. The formation of inactive Mg led to changes in the local current distribution and forced vertical Mg growth. Afterward, the uneven Mg deposits continued forming coral-like structures for up to 150 cycles, as shown in Figure 3h and Video S1. Until this stage, the galvanostatic cycling exhibited a uniform voltage profile ±0.25 V vs. $Mg|Mg^{2+}$ that maintained for 210 cycles as shown in Figure 3i, where each colored bullet point corresponds to its perspective optical image. Additionally, the zoomed-in galvanostatic cycling plots with green, purple, blue, and brown show the voltage profile after 50, 100, 150, and 200 cycles, indicating no further changes (see Figure 3j–m).

Thereafter, the microscope focus was switched to the left side at the corner, where the distance between both electrodes was

16146840, 0, Downloaded from https://advanced.onlinelibrary.wiley.com/doi/10.1002/aenm.202505315 by Karlsruher Institut Für Technologie, Wiley Online Library on [04/12/2025]. See the Terms and Conditions (https://onlinelibrary.wiley.com/terms-and-conditions) on Wiley Online Library for rules of use; OA articles are governed by the applicable Creative Commons License

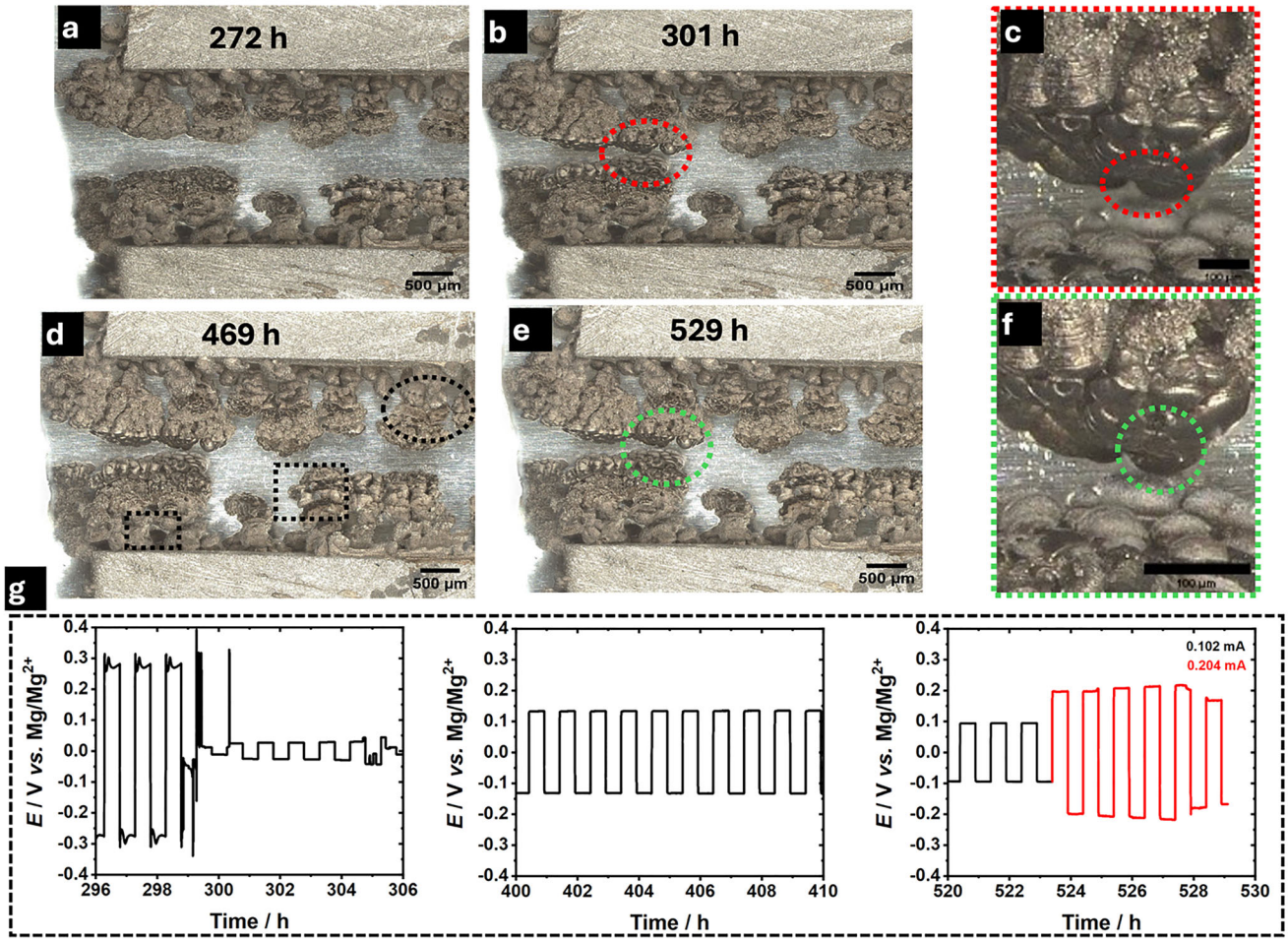

FIGURE 4 | (a–f) *Operando* optical microscopy images for the Mg|Mg cell operating at an apparent current density of 0.12 mA cm^{-2} at different times, focusing on the cell corners, where on each image the exact time is indicated as well as red, black and greendotted-circles or rectangles highlight the short circuit and the surface changes after the short circuit, respectively. The red and green-framed images are a zoom-in of the previous image; (g) Galvanostatic cycling of the symmetric Mg cell at different stages.

narrower by 0.25 mm as observed in Figure S1. The coral- or mossy-like structure continues growing for up to cycle number 300 without any significant changes in the voltage profile, as illustrated in Figure 4a. The mossy-like dendrites grown on both electrodes upon further cycling finally interconnected, causing a short circuit as shown in Figure 4b (also in Video S2). At this point, a significant voltage drop to a value of ±0.025 V vs. $Mg|Mg^{2+}$ was observed (see the corresponding galvanostatic cycling in Figure 4g). Further, the cell was kept under operation after the short circuit was reached to investigate the cell healing process under operating conditions. Interestingly, after approximately 170 h from the short circuit, some regions started to reactivate and white deposits and some cracks in the coral structure started to appear, as black-marked in Figure 4d (also see Video S3). At this stage, the voltage profile of the galvanostatic cycling went up to ±0.1 V vs. $Mg|Mg^{2+}$, as displayed in the corresponding galvanostatic cycling in Figure 4g. Later, the voltage profile dropped significantly again to ±0.0125 V vs. $Mg|Mg^{2+}$, indicating another internal short circuit, as displayed in Figure S2. Similarly, after 50 more cycles, another crack appeared at the junction between dendrites, as shown in Figure 4f,g. The voltage profile went up to ±0.1 V vs. $Mg|Mg^{2+}$ again, then the galvanostatic cycling profile remained stable as presented in Figure 4g. In the final six cycles, the applied current was doubled to test the cell response; this led to a notable increase in the voltage profile to ±0.2 V vs. $Mg|Mg^{2+}$, nearly restoring the initial voltage profile.

Unlike the results obtained with the BOLA cells, the reformation of Mg dendrites was observed in the optical microscopy, indicating a decisive effect of cell pressure and cell geometry.

2.2 | Mg Deposition/Stripping at High Current Densities

Since the relatively low current density of ±0.1 mA cm^{-2} resulted in a non-uniform deposition causing dendrites, in the next step, we investigated the impact of the applied current on dendrite formation or aversion. As previously discussed and illustrated in Figure 2a, at low current densities of ±0.1 mA $cm^{-2,}$ stable cycling was observed with a slight increase in the overpotential up to 120–135 cycles before an internal short circuit occurred, confirming the formation of soft dendrites. Increasing the current density by a factor of five to ±0.5 mA cm^{-2} (see Figure 5a), the overpotential scarcely increased compared to the behavior at 0.1 mA $cm^{-2,}$ and the cycling was stable for 25 cycles. Afterward,

16146840, 0, Downloaded from https://advanced.onlinelibrary.wiley.com/doi/10.1002/aenm.202505315 by Karlsruher Institut Für Technologie, Wiley Online Library on [04/12/2025]. See the Terms and Conditions (https://onlinelibrary.wiley.com/terms-and-conditions) on Wiley Online Library for rules of use; OA articles are governed by the applicable Creative Commons License

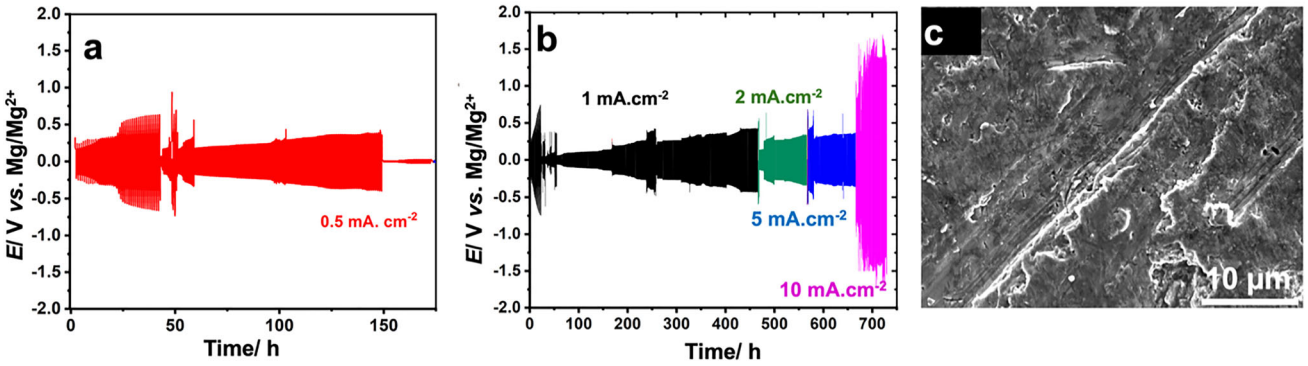

FIGURE 5 | Galvanostatic cycling of the Mg|Mg symmetric cell at (a) 0.5 mA cm^{-2}, (b) 1, 2, 5, 10 mA cm^{-2}, and (c) SEM micrograph of the Mg electrode after galvanostatic cycling shown in b.

the overpotential doubled until it reached ±0.5 V vs. $Mg|Mg^{2+}$ for another 25 cycles. Then, irregularities in the voltage profile could be observed, followed by a stable cycling with a voltage profile varying at ±0.25 V vs. $Mg|Mg^{2+}$ for 90 cycles with a minor increase in the overpotential, due to uneven Mg deposition and formation of inactive Mg. Thereafter, similar to the ±0.1 mA cm^{-2} measurement, a short circuit occurred after 150 cycles with a sudden drop in the cell voltage. Surprisingly, upon operating the cell at ±1 mA cm^{-2}, the galvanostatic cycling showed an improved voltage profile upon cycling, then stabilized for approximately 400 cycles without any signs of internal short circuit. Afterward, with the same cell, the current was doubled to ±2 mA cm^{-2}, then to 5 mA cm^{-2}, where stable cycling for 100 cycles at each current was observed with a voltage profile around ±0.35 V vs. $Mg|Mg^{2+}$. Further current density increase to ±10 mA cm^{-2} led to a significant increase of the overpotential to ±1.5 V vs. $Mg|Mg^{2+}$, with a stable cycling behavior for 100 more cycles (see Figure 5b). The electrodes were then extracted from the cell and analyzed by SEM. As depicted in Figure 5c, the surface appears smooth and homogeneous compared to the measurements at low current densities.

As for the cells operated at lower current densities, in the next step *operando* optical microscopy measurements were carried out at 6.67 mA cm^{-2}. The observed behavior is summarized in Figure 6 and Figure S3, which were recorded in Video S4. Surface activation was more pronounced in the first few cycles, and an extensive deposition rate could be achieved compared to the low current density case. Unlike the measurement at lower currents, uniform, smooth, and granular Mg deposits were formed during the initial cycles, as shown in Figure 6. This phenomenon is in good agreement with a previously reported study for Li [53], where smaller and smoother Li deposits were formed upon increasing the current density [53]. Tracking the Mg microstructure evolution during the first 2 h provides information about the initial nucleation. As shown in Figure 6, a uniform Mg deposition could be observed during the first 10 min that fully covered the whole Mg's cross section, followed by an increase in its thickness with time until the first full deposition cycle was completed. Increasing the deposition/stripping rate triggers extensive surface diffusion of Mg adatoms, resulting in spreading Mg deposits in a uniform layer. During the stripping process, the surface of the WE was not fully restored, while Mg deposition began at the CE. In the second deposition cycle, the undissolved Mg layer deposited from the previous cycle on the WE served as nucleation sites for subsequent Mg growth, with no change in the morphology of the deposited particles. Meanwhile, larger deposited particles formed on the Mg sheet's surface, and reversibly disappeared completely by the end of the second stripping, whereas the initial deposition layer at the sheet's edge persisted and remained undissolved throughout the experiment, which might refer to a stable SEI layer.

For up to 30 h, this uniform Mg deposition continued growing on both electrodes during the forward and reverse scans, as shown in Figure S3a. A slightly higher overpotential occurred compared to the measurements at lower current densities, as shown in Figure 3. Upon further cycling, the Mg deposits tend to increase at the nearer sides of the electrodes due to imperfectly aligned Mg electrodes. Since the cell is assembled inside the glovebox, ensuring the perfect position of both Mg electrodes is exactly parallel to each other is highly challenging. This causes an inhomogeneous electric field distribution with higher values at the corners, preferring deposition at the corners compared to the central region, as displayed in Figure S3f–h. With further cycling, the galvanostatic measurements showed a higher overpotential of ±0.6 V vs. $Mg|Mg^{2+}$ compared to the behavior at lower current densities, with a slight increase up to ±0.75 V vs. $Mg|Mg^{2+}$, as shown in Figure S3j–m. Therefore, one can conclude that higher current densities lead to a more uniform Mg deposition, while coral-like Mg deposits that might facilitate internal short circuit in our system can be avoided. However, 6.67 mA cm^{-2} is already a rather high current density that led to significant surface changes, particularly with long cycling. This suggests that a current density between 1 and 5 mA cm^{-2} might be a good compromise between system stability and efficiency.

To validate that (comparably) higher current densities are preferred in IL-based Mg batteries, a cell of $Mg|TiS_2$ was studied as a comparison, and its cycling stability was investigated at different specific current rates as well. The first cycle in CV showed two reduction and three oxidation peaks (see Figure 7a). Mg intercalation into the layered TiS_2 structure took place at 1.5 and 1.3 V, followed by Mg deintercalation at 1.5, 1.8, and 2.2 V vs. $Mg|Mg^{2+}$ in the reverse scan. On the other hand, the charge/discharge profile of TiS_2 at different current rates showed a notable decrease in the capacity after the first cycle, as shown in Figure 7b, which is also in agreement with previous studies on TiS_2 [27, 30, 54]. During

16146840, 0, Downloaded from https://advanced.onlinelibrary.wiley.com/doi/10.1002/aenm.202505315 by Karlsruher Institut Für Technologie, Wiley Online Library on [04/12/2025]. See the Terms and Conditions (https://onlinelibrary.wiley.com/terms-and-conditions) on Wiley Online Library for rules of use; OA articles are governed by the applicable Creative Commons License

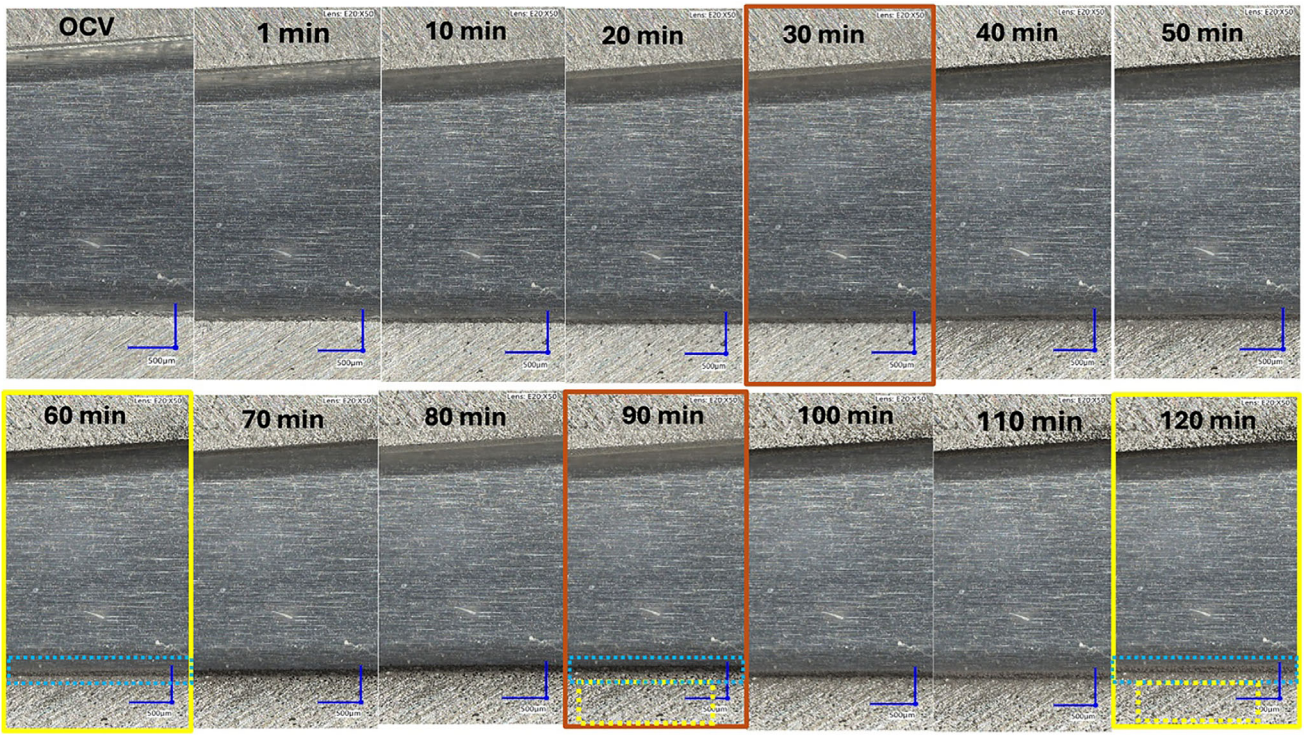

FIGURE 6 | Optical microscopy images of the Mg|Mg cell operated at 6.67 mA cm^{-2} during the first two cycles. Orange- and yellow-framed images are for the surface at full deposition and full stripping stages, respectively.

the first cycle of Mg intercalation/deintercalation, an irreversible phase transformation occurred, accompanied by capacity loss in the subsequent cycling, where a partial Mg deception within the TiS_2 structure took place due to the influence of Mg^{2+} ion kinetics as well as complex ordering [27, 30]. Thus, in Figure 7b the voltage profiles of the second cycle at different specific current rates (100, 80, 50, 30, 20, 10, 5, and 2 mA g^{-1}) were plotted, and specific capacities of 7.5, 62, 65, 68, 73, 101.5, 200 mAh g^{-1} were achieved, respectively.

To further investigate this phase transformation, post-mortem analyses, such as XRD, SEM, and elemental mapping, were utilized. As illustrated in Figure 7c, the XRD pattern shows that after the discharge process, the peak at 17.1° disappears, and the intensity of the peak at 28.5° decreases significantly after discharging and charging, confirming the structural change in TiS_2 from phase 1 to phase 2/3 [27, 30]. Further, the SEM micrographs displayed in Figure 7d demonstrate a platelet morphology without any significant morphological changes before and after discharging or charging processes. Interestingly, in Figure 7e, the SEM micrograph (with higher magnification) for a tilted sample after the second discharging process shows the clear layered structure of TiS_2, and the elemental mapping shows the homogeneous distribution of Ti, S, and Mg inserted inside the layered structure. Herein, it is worth highlighting the importance of performing all the preparation processes from the electrode slurry to cell assembly inside the glove box. All the trials to fabricate the electrode outside the glovebox, followed by the conventional drying under vacuum, were not successful in avoiding the drastic effect of water traces that resulted in unsuccessful Mg intercalation, as shown in Figure S4.

Furthermore, the cyclic stability of TiS_2 (prepared inside the glovebox) was investigated at different current rates from a relatively low specific current of 10 mA g^{-1} to a relatively high specific current rate of 50 mA g^{-1}, as displayed in Figure 7f,g and Figure S5. Interestingly, higher stability, coulombic efficiency, and capacity retention could be achieved at the high specific current rate of 50 mA g^{-1} (see Figure 7f), where the capacity retention of the initial capacity is 80% after 50 cycles. Further, as demonstrated in Figure 7g, the lower the specific current rate, the lower the capacity retention achievable. Surprisingly, after 30 cycles of operation at 10 mA g^{-1}, an irregularity occurred during the charging process, indicating the occurrence of soft dendrites that resulted in a significant drop in capacity retention, as apparent in Figure S5b. From Figure 7f,g and Figure S5b, it is clear that selecting safe operating currents has a significant influence on the suppression of dendrites and on achieving high cycle stability. Additionally, increasing the current rate enhances the stripping homogeneity, which is associated with an increase in the concentration of the Mg salts constituents and their distribution on the interface, resulting from faster reaction rates as well as higher polarization concentration [17, 55].

Based on the previous insights from the electrochemical and optical microscopy investigations, the discrepancy of applied current density and dendrite formation in previously reported studies, as illustrated in Table S1, seems to be related mainly to the actual active surface area, local current density, operating conditions, and electrolyte composition. Consequently, the use of terms such as “low” or “high” currents requires re-evaluation. Defining safe operating conditions and the critical current density (CCD) is essential. Notably, mitigation strategies such as artificial

16146840, 0, Downloaded from https://advanced.onlinelibrary.wiley.com/doi/10.1002/aenm.202505315 by Karlsruher Institut Für Technologie, Wiley Online Library on [04/12/2025]. See the Terms and Conditions (https://onlinelibrary.wiley.com/terms-and-conditions) on Wiley Online Library for rules of use; OA articles are governed by the applicable Creative Commons License

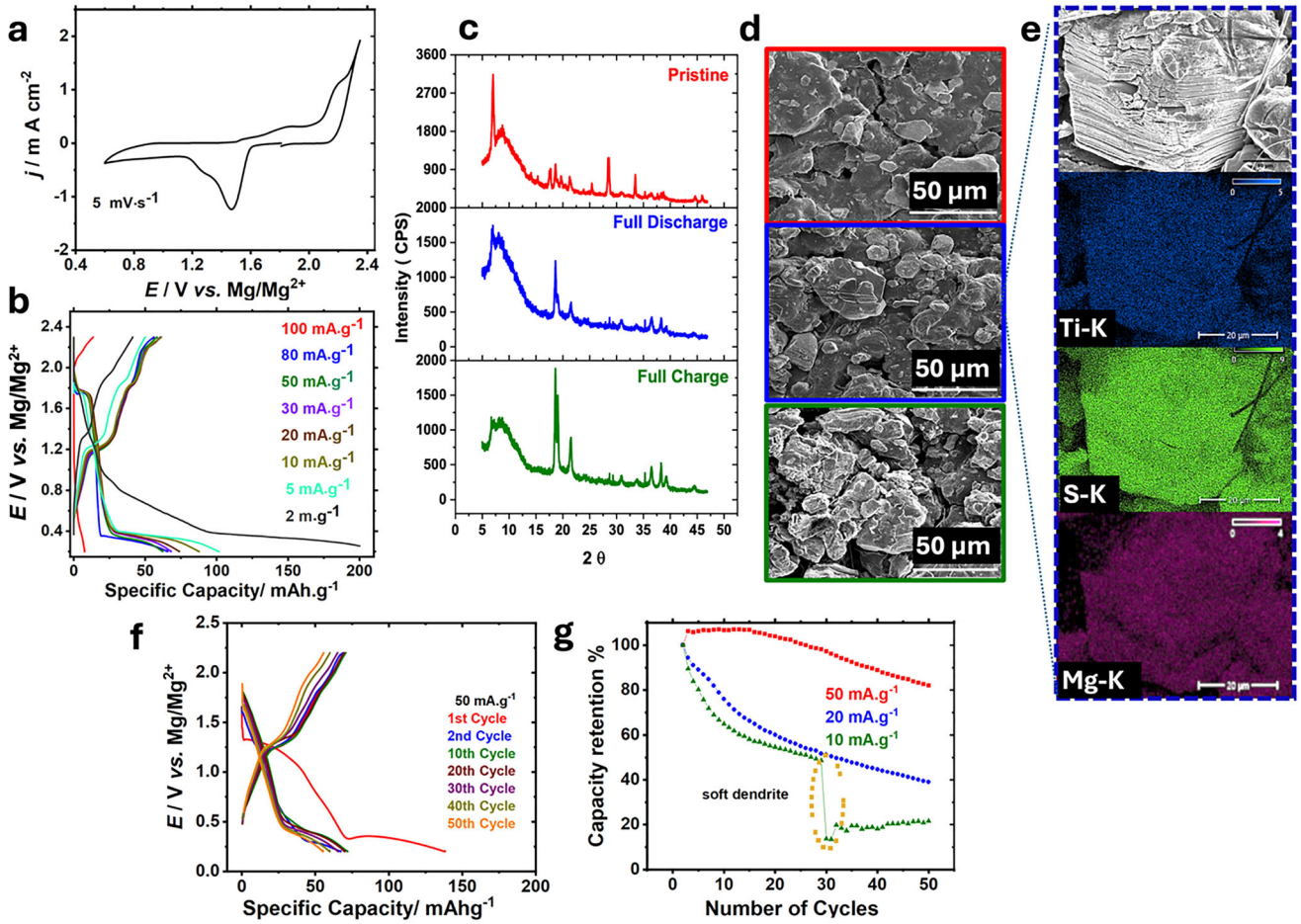

FIGURE 7 | (a) Cyclic voltammetry of the Mg|TiS_2 cell at a scan rate of 5 mV s^{-1}; (b) Charge–discharge profile of TiS_2 at different current densities; (c) XRD pattern for TiS_2: pristine, after a full discharge, and after full charge; (d) The corresponding SEM micrographs; (e) SEM micrograph and the corresponding elemental mapping of TiS_2 at full discharge showing its layered structure; (f) Stability of TiS_2 electrode up to 50 cycles at 50 mA g^{-1}; and (g) Capacity retention vs. number of cycles for the cells operated at different current densities of 50, 20, 10 mA g^{-1}.

interphases and anode modifications have successfully promoted uniform Mg deposition, thereby suppressing dendrite growth, as detailed in Table S1. However, some of these reports did not show an extensive number of cycles to prove the potential of their mitigation strategies, where 90 or 100 cycles are not sufficient to prove the absence of dendrites. Thus, understanding the factors affecting Mg deposition from each system should be the first step toward a successful mitigation strategy for dendrite-free Mg batteries.

2.3 | Mg Dendrites Growth and Cell Healing Mechanisms

To understand the Mg dendrite formation mechanism in the MIDS electrolyte, it is essential to understand the role of each component and the limiting process/processes governing the Mg deposition process. Eom et al. showed that the cations of the ionic liquid adsorb on the anode surface as well as on freshly deposited Mg. In the presence of high donor number (DN) co-solvents (such as glymes), the co-solvent molecules prefer occupying the metal ion's solvation sheath, promoting organic cation–anion association that prevents decomposition of the organic cations [56]. Adsorption of the protected IL cations expels the upcoming Mg^{2+} ions away from the tips. This results in an electrostatic shielding effect that accelerates the lateral deposition and consequently a stable interphase [57]. At the same time, $Mg(BH_4)_2$ modifies the solvation structure, neutralizing the formed active intermediate Mg^{2+} clusters, which results in the formation of a highly stable SEI and consequently a reversible Mg deposition/stripping process [58]. Moreover, the adsorption of active clusters was found to be the vital step toward reversible Mg deposition and stripping [58, 59], which at the same time limits dendrite growth as well as any morphological surface changes [60]. Combining previous findings with our results provides a clear picture of the formation of Mg dendrites at low and high currents and their disappearance upon cycling in our system, while they remain in other systems. Since the adsorption of protected active clusters is vital to achieve a uniform deposition, the adsorption rate will be highly dependent on the current value. At low currents, i.e., low electric fields, the adsorption affinity is reduced, with a high competition between adsorption of active Mg^{2+} clusters and the occurrence of reduction processes, resulting in low surface coverages and a non-uniform deposition. In contrast, at high currents, i.e., high electric fields, ion diffusion is enhanced, increasing the adsorption rate and resulting in a faster deposition and a Mg electrode fully covered with adsorbed protected IL-cations. This adlayer facilitated lateral

16146840, 0, Downloaded from https://advanced.onlinelibrary.wiley.com/doi/10.1002/aenm.202505315 by Karlsruher Institut Für Technologie, Wiley Online Library on [04/12/2025]. See the Terms and Conditions (https://onlinelibrary.wiley.com/terms-and-conditions) on Wiley Online Library for rules of use; OA articles are governed by the applicable Creative Commons License

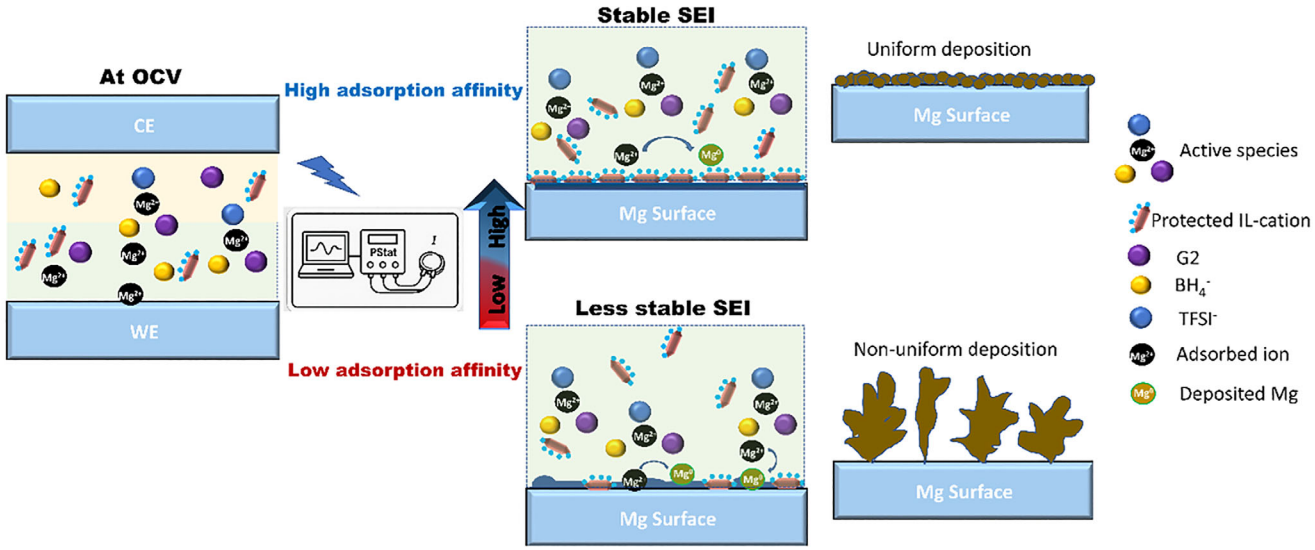

SCHEME 1 | Mechanism of Mg dendrite growth showing the difference between applying low and high current rates.

deposition, resulting in a more uniform deposition as shown in Scheme 1.

In order to investigate the reasons behind the observed cell-healing, a chronoamperometry measurement was conducted to investigate current flow during the internal short circuit in a magnesium-based electrochemical cell. The potential was cycled between −0.4 and 0.4 V vs. Mg|Mg^{2+}, and the current was recorded over time (see Figure 8). In the initial cycles, the current reached ±4 mA, stabilizing at plateaus of ±0.2 mA. Upon cycling, both features (the maximum as well as the plateau currents) decrease as a result of the formation of an SEI layer, resulting in a change in cell impedance. After 80 cycles, a sudden current spike to +100 and −60 mA was observed, coinciding with corresponding in situ EIS measurements (Figure S6b), indicating an internal short circuit. Achieving a very low resistance at the short circuit and after dendrite formation results in a non-controllable increase in the local currents and consequently an increase in the local temperature due to self-heating. The elevated local temperature facilitates cell recovery from soft dendrites via dendrite fusion, indicating a self-healing mechanism as illustrated in Figure 8c. Here, we consider the fusion of Mg deposits with particle sizes in the submicron range. At such scales, the melting point is significantly lowered owing to the high surface-to-volume ratio, where surface atoms experience fewer neighboring interactions and thus reduced cohesive forces. This process enables dendrite recovery and cell self-healing through atomic migration and defect relaxation at deposit interfaces and tips. Surface and grain boundary diffusion govern mass transport, permitting atoms to migrate from high-curvature regions (dendrite tips) to lower-curvature areas, thereby promoting morphological smoothing and electrical reconnection.

In a previous study by Ding et al., the formation of Mg dendrites was recorded after 320 cycles in a symmetric Mg cell using 0.3 M $Mg(TFSI)_2$/diglyme as electrolyte [11]. At the short circuit, a cell voltage profile of ±0.002 V vs. Mg|Mg^{2+} was observed, and the short circuit persisted for up to 2000 cycles, indicating cell failure. In contrast, in our study, the healing of the short circuit was achieved and upheld up to 500 cycles. The incorporation of MPPip-TFSI ionic liquid and $Mg(BH_4)_2$ into the electrolyte likely facilitated cell recovery. These additives altered the physicochemical characteristics of the glyme-$Mg(TFSI)_2$-containing electrolytes, enhancing anodic stability to better tolerate abrupt changes in local current and temperature without degrading.

In order to prove the thermally-induced self-heating assumption, symmetric Mg|Mg cells operated at 0.1 mA cm^{-2} and stopped right after the short circuit were subjected to an annealing process at different temperatures. The first cell was annealed at 80°C for 72 h, then EIS and SEM were recorded to track the surface changes (see Figure S7). The Nyquist plot after the annealing process showed an increase in the cell impedance as well as a diffusion tail in the low-frequency region, indicating cell healing. This is in agreement with other reports on lithium-based systems that showed healing from dendrites after cell annealing at 70°C–80°C [45, 61]. However, in our case, when the cell was operated again at the same current density, the previous voltage profile could not be fully restored, and the cell stopped after a few cycles due to passivation. This suggests that the annealing process for three days at 80°C resulted in parasitic side reactions and accelerated electrolyte decomposition, and consequently passivated the Mg electrode. Both dendrite fusion and electrolyte decomposition after cell annealing at 80°C could be confirmed by SEM imaging and elemental mapping (see Figure S7e). The SEM micrograph showed a complete fusion of Mg dendrites. At the same time, an increase in S, F, N, and C elemental concentrations can be observed in some regions as an indication of electrolyte decomposition.

The second cell that was stopped at the short circuit was annealed, but this time at a lower temperature and for a much shorter time (40°C for 24 h). The Nyquist plot after cell annealing again exhibited an increase in cell impedance with the appearance of a diffusion tail in the low-frequency region, indicating the restoration of an electric connection and, consequently, the cell healing from dendrites. Figure 9a displays the SEM micrograph of the electrode after annealing for 24 h at 40°C, where the

16146840, 0, Downloaded from https://advanced.onlinelibrary.wiley.com/doi/10.1002/aenm.202505315 by Karlsruher Institut Für Technologie, Wiley Online Library on [04/12/2025]. See the Terms and Conditions (https://onlinelibrary.wiley.com/terms-and-conditions) on Wiley Online Library for rules of use; OA articles are governed by the applicable Creative Commons License

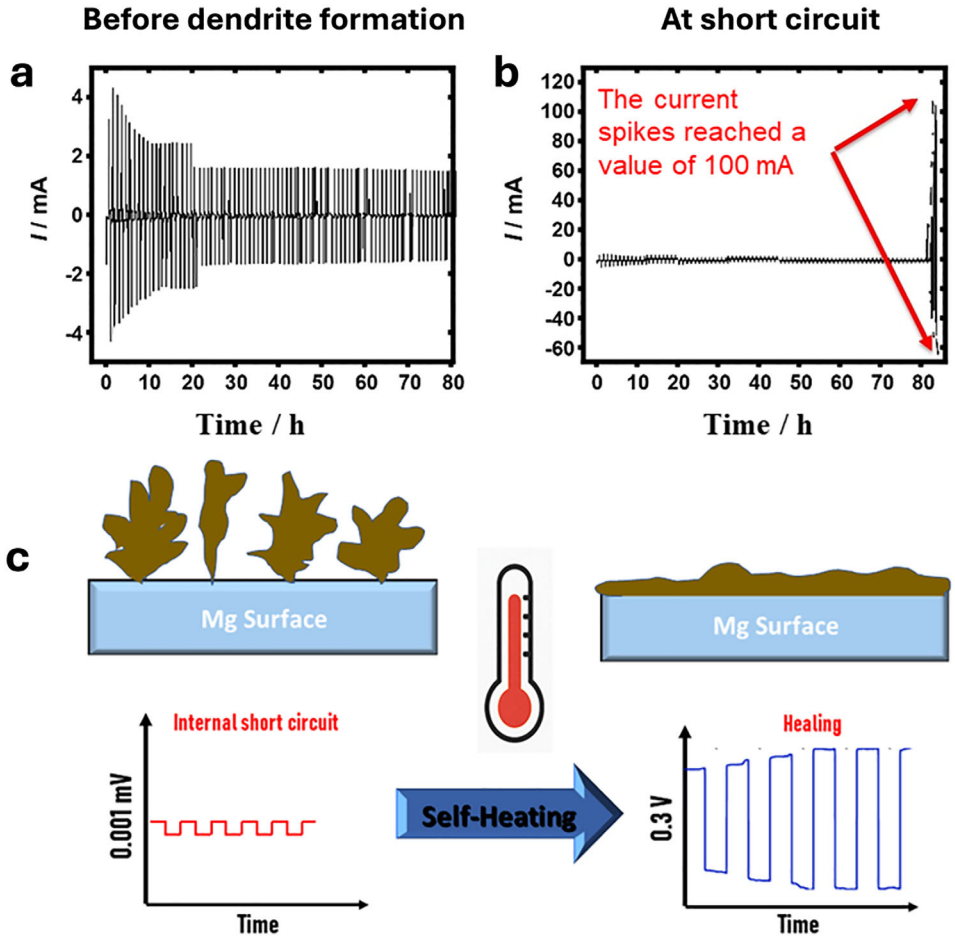

FIGURE 8 | Chronoamperometry study of a symmetric Mg|Mg cell measured at RT using a constant potential of ±0.4 V: (a) Current profile before the short circuit, (b) current profile showing the current spikes at the short-circuit, and (c) sketch of the proposed self-healing mechanism.

fusion of Mg dendrites could be observed. After annealing, the cell was operated again at room temperature under the same current density (0.1 mA cm^{-2}) to test whether or not the cell performance was restored. As shown in Figure 9b, at the beginning of the reoperation, Mg deposition/stripping was possible again and the cell impedance was restored (see Figure 9c). Afterward, the voltage profile showed some irregularities and a dynamic change in the overpotential before it stabilized after approximately 75 cycles. No further change in the cell impedance was recorded; rather the Nyquist plots showed a stable behavior for up to 350 cycles. This suggests a perturbation in the SEI after annealing that got stabilized upon further cycling [62].

Furthermore, in order to investigate whether or not a higher temperature is preferred in our system to obtain a stable dendrite-free cycling, a freshly-assembled symmetric Mg|Mg cell was operated at 40°C (see Figure S8a). The overpotential for Mg deposition/stripping was comparable to that measured at room temperature, with a gradual increase in the overpotential observed upon cycling. Notably, irregularities in the voltage profile persisted for nearly 90 cycles. After approximately 30 cycles, a temporary drop in both the voltage and cell impedance was observed, followed by a recovery. A similar but more pronounced drop occurred around cycle 70. At this stage, the Nyquist plot (Figure S8f) did not indicate a short circuit but rather showed two distinct semicircles with a total resistance of approximately 300 Ω, which is attributed to the growth of an SEI. Around 20 cycles later, the voltage profile began increasing again, accompanied by a significant change in the Nyquist plot: a diffusion tail emerged in the low-frequency region, indicating a mass transport limitation. This behavior could be associated with the formation of inactive Mg, the growth of Mg dendrites, or partial surface passivation that blocks active sites and increases impedance. With continued cycling, a partial regeneration of the electrode surface led to a stabilization of the voltage profile, retaining the impedance shape, although the overall cell impedance continued rising, suggesting a progressive thickening of the SEI layer.

3 | Conclusion

In summary, we systematically investigated the influence of current density on dendrite growth mechanisms in symmetric Mg|Mg as well as asymmetric Mg|TiS_2 cells. The applied current density shows a direct correlation with the morphology of the deposited magnesium: at low current densities (0.01–0.5 mA cm^{-2}), non-uniform, coral-like Mg deposits were formed, which promoted the growth of soft dendrites, finally causing a short circuit. In contrast, higher currents (1–5 mA cm^{-2}) resulted in uniform spherical Mg deposits with a stable cycling up to 700 cycles. *Ex situ* characterization and *operando* optical microscopy provided detailed insights into the nucleation and growth of the

16146840, 0, Downloaded from https://advanced.onlinelibrary.wiley.com/doi/10.1002/aenm.202505315 by Karlsruher Institut Für Technologie, Wiley Online Library on [04/12/2025]. See the Terms and Conditions (https://onlinelibrary.wiley.com/terms-and-conditions) on Wiley Online Library for rules of use; OA articles are governed by the applicable Creative Commons License

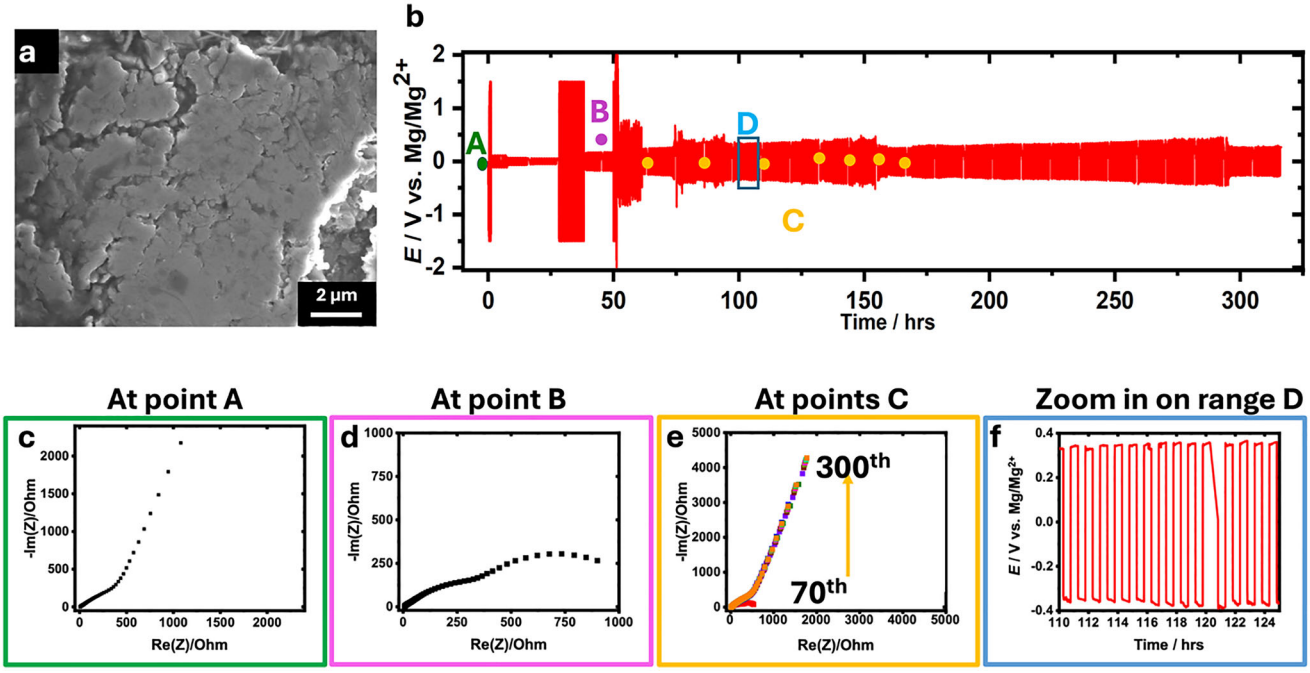

FIGURE 9 | (a) SEM micrograph of the Mg electrode in the dendritic cell after annealing at 40°C for 24 h; (b) Galvanostatic behavior of the symmetric Mg|Mg cell operated at 0.1 mA cm^{-2} after recovering from dendrites due to annealing at 40°C for 24 h; (c) Nyquist plot of the cell directly after annealing at 40°C for 24 h; (d) Nyquist plot at point B; (e) Nyquist plots of the cell during the last 230 cycles at points C, where an EIS spectrum was recorded every 20 cycles; (f) Enlarged voltage profile on the D range.

Mg deposits. Furthermore, our investigations on the asymmetric Mg|TiS_2 cell highlighted the impact of higher specific current rates (50 mA g^{-1}) on cyclic stability, contrasted to failure due to soft dendrites at 10 mA g^{-1}. Further, at 50 mA g^{-1} and after 50 cycles, 80% of the initial capacity is maintained with a coulombic efficiency of about 100%, while a high specific capacity of 200 mAh g^{-1} at 2 mA g^{-1} could be obtained. Interestingly, after the occurrence of a soft dendrite-induced short circuit, cells recovered by means of further cycling, with dendrite fusion demonstrated via SEM imaging. Those findings contribute to deeper insights and understanding of the mechanism of dendrite formation in Mg batteries that can show a self-healing behaviour under certain conditions. This study emphasizes the critical impact of electrolyte constituents and electrochemical parameters on dendrite formation and cell recovery, which offers a route to develop safer and more durable rechargeable batteries.

4 | Experimental Section

4.1 | Chemicals

1-Methyl-1-propylpiperidinium bis(trifluoromethylsulfonyl)imide (MPPip-TFSI) IL (>99% purity, water content <100 mg L^{-1} and halides <100 mg L^{-1}) was bought from Iolitec. Diglyme (G2) (99.5%), magnesium borohydride ($Mg(BH_4)_2$, 95%), and titanium disulfide (TiS_2, 99.9%) were purchased from Sigma–Aldrich. Magnesium(II) bis(trifluoromethanesulfonyl)imide ($Mg(TFSI)_2$, 99.5%) was obtained from Solvionic. Carbon black was ordered from the Cabot corporation. Additionally, poly (vinylidene fluoride) (PVDF) was bought from Alfa Aesar. N-Methyl-2-pyrrolidone (NMP) ≥99% was purchased from VWR chemicals. Diglyme was pre-dried over 4 Å molecular sieves for one week before mixing with the ionic liquid. $Mg(TFSI)_2$ was dried for 16 h at 120°C under vacuum, then stored in the glovebox, whereas $Mg(BH_4)_2$ was used as received without additional drying.

4.2 | Electrolyte Preparation

The electrolyte used in our measurements was the optimized electrolyte reported in our previous study [41]. It was composed of 0.1 M $Mg(TFSI)_2$ and 0.01 M $Mg(BH_4)_2$ dissolved in 1:3 MPPip-TFSI:diglyme. Briefly, MPPip-TFSI ionic liquid was dried by using 4 Å molecular sieves at 80°C for 20 h under a low pressure of 10^{-3} mbar. The detailed drying method was reported in our previous study [20]. Inside an Ar-filled LABStar glovebox from mBRAUN (O_2 and H_2O level ≤ 0.5 ppm), diglyme was mixed with MPPip-TFSI in a volume ratio of 3:1 before adding the corresponding amounts of $Mg(TFSI)_2$ and $Mg(BH_4)_2$. The mixture was then stirred overnight at 40°C to obtain a clear solution, then stored inside the glovebox for further use. For simplicity, the abbreviation MIDS was used throughout the manuscript to refer to our optimized magnesium ionic liquid-diglyme-Mg salt electrolyte.

4.3 | TiS_2 Cathode Electrode Preparation

Commercial TiS_2 powder (CAS-No:12039-13-3) was used as received without any pre-treatment. Inside the glovebox, TiS_2 electrodes were fabricated by mixing the active material (TiS_2) with carbon black and PVDF in NMP solvent in a weight ratio of 80:10:10, respectively. The mixture was then stirred until a

16146840, 0, Downloaded from https://advanced.onlinelibrary.wiley.com/doi/10.1002/aenm.202505315 by Karlsruher Institut Für Technologie, Wiley Online Library on [04/12/2025]. See the Terms and Conditions (https://onlinelibrary.wiley.com/terms-and-conditions) on Wiley Online Library for rules of use; OA articles are governed by the applicable Creative Commons License

homogeneous slurry was obtained. Further, the slurry was coated on an Al foil by using a doctor blade placed inside the glovebox, having an average active mass of 2.3 mg. Similarly, a slurry of the same components was prepared in a fume hood for comparison. Thereafter, the coated foils were dried in a vacuum oven at 120°C for 2 h, then at 80°C for 12 h. Further, the foil was cut down into ∅12 mm disks and stored in the glovebox for further use. The electrodes that have been prepared outside the glovebox were subjected to further drying in a Büchi glass oven at 70°C for 2 h before transferring to the glovebox. All measurements were carried out at RT. The galvanostatic cycling was performed at different current rates ranging from 2 to 100 mA g^{-1} in the voltage range from 0.2 to 2.3 V. The cycling stability was performed in the same voltage range at different current rates of 50, 20, and 10 mA g^{-1}, each for 50 cycles.

4.4 | Structural Characterization

The scanning electron microscope (SEM) imaging and energy dispersive X-ray spectroscopy (EDX) measurements were carried out using an Apero 2 from Thermo Fisher Scientific. A clean connect set-up was utilized to transfer the samples from the glovebox to the SEM without air exposure.

X-ray powder diffraction (XRD) patterns were recorded on a STOE Stadi P diffractometer with the following conditions: Cu-Kα radiation ($\lambda = 0.154$ nm; 40 kV, 40 mA) using the transmission mode. The electrodes were assembled in the sample holder inside the glovebox to avoid air exposure and covered by Kapton. The reflection mode was used to measure the XRD of the coated electrodes.

4.5 | Operando Optical Microscopy (OM)

Operando microscopy was conducted using a Keyence VHX-7000 digital microscope. A Palmsens potentiostat was utilized for the galvanostatic charging and discharging of a custom-fabricated pouch cell, which featured an integrated transparent glass window. Prior to assembly, the edges of two magnesium metal sheets (1.0 mm thick) were mechanically polished to remove any surface oxide layer. Aluminum tabs were ultrasonically welded to the magnesium metal electrodes to function as current collectors. The symmetric magnesium pouch cell was cycled at two different constant currents of 102.8 or 822.4 µA, which were reversed every 30 min for a total number of 500 and 200 cycles, respectively. Images were taken under 50-fold magnification every minute during electrochemical cycling.

4.6 | Electrochemical Characterization

Galvanostatic cycling and electrochemical impedance spectroscopy (EIS) were conducted in a BOLA cell, similar to a Swagelok, but with an outer lining made of Teflon, using a PG2 potentiostat from BioLogic. Galvanostatic cycling was conducted at different currents ranging from 0.01 to 10 mA, which were reversed every 30 min. Further, the EIS was recorded with an AC amplitude of 10 mV in the frequency range from 100 kHz to 100 mHz. In the symmetric Mg|Mg cell, magnesium sheets (HMW Hauner GmbH, 99.8%) with a diameter of ∅12 mm and a thickness of 0.1 mm were used as counter and working electrodes, respectively. Both surfaces of the sheet were polished with sandpaper to remove any oxide layer. One Whatman (GF/B) glass fiber separator soaked with 70 µL of our MIDS electrolyte was placed between both Mg electrodes. For the asymmetric Mg|TiS_2 cell, TiS_2 was used as the working electrode and a Mg sheet as the counter electrode. The cells were kept at the open circuit voltage (OCV) and at room temperature for 12 h before starting any measurement. Cycling voltammograms (CV) were recorded at a scan rate of 5 mV s^{-1} in a potential window from 0.6 to 2.3 V. Galvanostatic cycling was measured at current densities ranging from 2 to 100 mA g^{-1} in a potential window from 0.2 to 2.5 V. All measurements of the asymmetric cells were recorded at 25°C. The cells were placed in a climate chamber (KB 115, Binder, ± 0.1°C) to keep a constant temperature throughout the measurements Mg batteries.

Acknowledgements

The authors gratefully acknowledge funding by the DFG (Deutsche Forschungsgemeinschaft) through research unit FOR-5065 (id 428906592) and project 501805371, partial funding from the DFG under Germany's Excellence Strategy – EXC 2154 – Project number 390874152 (POLiS Cluster of Excellence). as well as by the BMBF (Bundesministerium fur Bildung und Forschung) through the project CASINO (FKZ: 03XP0487G) and the state of Baden-Württemberg and the DFG through grant no INST 40/574-1 FUGG.

Open access funding enabled and organized by Projekt DEAL.

Conflicts of Interest

The authors declare no conflicts of interest.

Data Availability Statement

The data that support the findings of this study are available from the corresponding author upon reasonable request.

References

1. A. Das, N. T. M. Balakrishnan, P. Sreeram, et al., "Prospects for Magnesium Ion Batteries: A Compreshensive Materials Review," *Coordination Chemistry Reviews* 502 (2024): 215593, https://doi.org/10.1016/j.ccr.2023.215593.

2. G. Wang, Z. Wang, H. Shi, A. Du, M. Sun, and G. Cui, "Progress and Perspective on Rechargeable Magnesium-ion Batteries," *Science China Chemistry* 67 (2024): 214–246, https://doi.org/10.1007/s11426-022-1454-0.

3. P. Saha, M. K. Datta, O. I. Velikokhatnyi, A. Manivannan, D. Alman, and P. N. Kumta, "Rechargeable Magnesium Battery: Current Status and Key Challenges for the Future," *Progress in Materials Science* 66 (2014): 1–86, https://doi.org/10.1016/j.pmatsci.2014.04.001.

4. M. K. Aslam, Y. Niu, T. Hussain, et al., "How to Avoid Dendrite Formation in Metal Batteries: Innovative Strategies for Dendrite Suppression," *Nano Energy* 86 (2021): 106142, https://doi.org/10.1016/j.nanoen.2021.106142.

5. Y. Zhang, J. Xie, Y. Han, and C. Li, "Dual-Salt Mg-Based Batteries With Conversion Cathodes," *Advanced Functional Materials* 25 (2015): 7300–7308, https://doi.org/10.1002/adfm.201503639.

6. J. Muldoon, C. B. Bucur, and T. Gregory, "Quest for Nonaqueous Multivalent Secondary Batteries: Magnesium and beyond," *Chemical Reviews* 114 (2014): 11683–11720, https://doi.org/10.1021/cr500049y.

16146840, 0, Downloaded from https://advanced.onlinelibrary.wiley.com/doi/10.1002/aenm.202505315 by Karlsruher Institut Für Technologie, Wiley Online Library on [04/12/2025]. See the Terms and Conditions (https://onlinelibrary.wiley.com/terms-and-conditions) on Wiley Online Library for rules of use; OA articles are governed by the applicable Creative Commons License

7. M. Matsui, "Study on Electrochemically Deposited Mg Metal," *Journal of Power Sources* 196 (2011): 7048–7055, https://doi.org/10.1016/j.jpowsour.2010.11.141.

8. Q. S. Zhao, Y. N. NuLi, Y. S. Guo, J. Yang, and J. L. Wang, "Reversibility of Electrochemical Magnesium Deposition From Tetrahydrofuran Solutions Containing Pyrrolidinyl Magnesium Halide," *Electrochimica Acta* 56 (2011): 6530–6535, https://doi.org/10.1016/j.electacta.2011.04.114.

9. T. Gao, S. Hou, K. Huynh, et al., "Existence of Solid Electrolyte Interphase in Mg Batteries: Mg/S Chemistry as an Example," *ACS Applied Materials & Interfaces* 10 (2018): 14767–14776, https://doi.org/10.1021/acsami.8b02425.

10. C. Ling, D. Banerjee, and M. Matsui, "Study of the Electrochemical Deposition of Mg in the Atomic Level: Why It Prefers the Non-dendritic Morphology," *Electrochimica Acta* 76 (2012): 270–274, https://doi.org/10.1016/j.electacta.2012.05.001.

11. M. S. Ding, T. Diemant, R. J. Behm, S. Passerini, and G. A. Giffin, "Dendrite Growth in Mg Metal Cells Containing $Mg(TFSI)_2$ /Glyme Electrolytes," *Journal of Electrochemistry Society* 165 (2018): A1983–A1990.

12. A. Hagopian, D. Kopač, J.-S. Filhol, and A. K. Lautar, "Morphology Evolution and Dendrite Growth in Li- and Mg-metal Batteries: A Potential Dependent Thermodynamic and Kinetic Multiscale Ab Initio Study," *Electrochimica Acta* 353 (2020): 136493, https://doi.org/10.1016/j.electacta.2020.136493.

13. J. H. Kwak, Y. Jeoun, S. H. Oh, et al., "Operando Visualization of Morphological Evolution in Mg Metal Anode: Insight Into Dendrite Suppression for Stable Mg Metal Batteries," *ACS Energy Letters* 7 (2022): 162–170, https://doi.org/10.1021/acsenergylett.1c02486.

14. R. Davidson, A. Verma, D. Santos, et al., "Formation of Magnesium Dendrites During Electrodeposition," *ACS Energy Letters* 4 (2019): 375–376, https://doi.org/10.1021/acsenergylett.8b02470.

15. L. Wang, P. C. P. Li, R. Family, and E. Detsi, "Magnesium Dendrite Growth During Electrodeposition in Conditioned Mg(TFSI)2/AlCl3/MgCl2/DME Electrolyte," *Journal of Nanoparticle Research* 26 (2024): 1, https://doi.org/10.1007/s11051-023-05905-0.

16. Y. Xiong, B. Yan, Q. Li, C. Zhi, and J. Fan, "Phase Field Modeling of Dendrite Growth Mechanism of Mg and Li in Electrodeposition," *Journal of Power Sources* 597 (2024): 234162, https://doi.org/10.1016/j.jpowsour.2024.234162.

17. X. Liu, A. Du, Z. Guo, et al., "Uneven Stripping Behavior, an Unheeded Killer of Mg Anodes," *Advanced Materials* 34 (2022): 2201886, https://doi.org/10.1002/adma.202201886.

18. J. Zhang, J. Liu, M. Wang, et al., "The Origin of Anode–electrolyte Interfacial Passivation in Rechargeable Mg-metal Batteries," *Energy & Environmental Science* 16 (2023): 1111–1124.

19. H. Kuwata, M. Matsui, and N. Imanishi, "Passivation Layer Formation of Magnesium Metal Negative Electrodes for Rechargeable Magnesium Batteries," *Journal of The Electrochemical Society* 164 (2017): A3229–A3236, https://doi.org/10.1149/2.1191713jes.

20. O. W. Elkhafif, H. K. Hassan, M. U. Ceblin, A. Farkas, and T. Jacob, "Influence of Residual Water Traces on the Electrochemical Performance of Hydrophobic Ionic Liquids for Magnesium-Containing Electrolytes," *ChemSusChem* 16 (2023): 202300421, https://doi.org/10.1002/cssc.202300421.

21. Z. Ma, D. R. MacFarlane, and M. Kar, "Mg Cathode Materials and Electrolytes for Rechargeable Mg Batteries: A Review," *Batteries & Supercaps* 2 (2019): 115–127, https://doi.org/10.1002/batt.201800102.

22. B. Wan, H. Dou, X. Zhao, et al., "Three-Dimensional Magnesiophilic Scaffolds for Reduced Passivation Toward High-Rate Mg Metal Anodes in a Noncorrosive Electrolyte," *ACS Applied Materials & Interfaces* 12 (2020): 28298–28305, https://doi.org/10.1021/acsami.0c07213.

23. Y. Li, S. Kumar, G. Yang, et al., "The Contrast Between Monovalent and Multivalent Metal Battery Anodes," *Science* 389 (2025): adl5482, https://doi.org/10.1126/science.adl5482.

24. B. Li, R. Masse, C. Liu, et al., "Kinetic Surface Control for Improved Magnesium-electrolyte Interfaces for Magnesium Ion Batteries," *Energy Storage Materials* 22 (2019): 96–104, https://doi.org/10.1016/j.ensm.2019.06.035.

25. G. Yang, Y. Li, C. Zhang, et al., "In Situ Formed Magnesiophilic Sites Guiding Uniform Deposition for Stable Magnesium Metal Anodes," *Nano Letters* 22 (2022): 9138–9146.

26. G. Yang, Y. Li, J. Wang, et al., "Realizing Horizontal Magnesium Platelet Deposition and Suppressed Surface Passivation for High-performance Magnesium Metal Batteries," *Energy & Environmental Science* 17 (2024): 1141–1152, https://doi.org/10.1039/D3EE02317F.

27. X. Sun, P. Bonnick, and L. F. Nazar, "Layered TiS_2 Positive Electrode for Mg Batteries," *ACS Energy Letters* 1 (2016): 297–301, https://doi.org/10.1021/acsenergylett.6b00145.

28. N. Amir, Y. Vestfrid, O. Chusid, Y. Gofer, and D. Aurbach, "Progress in Nonaqueous Magnesium Electrochemistry," *Journal of Power Sources* 174 (2007): 1234–1240, https://doi.org/10.1016/j.jpowsour.2007.06.206.

29. T. Gao, F. Han, Y. Zhu, et al., "Hybrid Mg^{2+} /Li^+ Battery With Long Cycle Life and High Rate Capability," *Advanced Energy Materials* 5 (2015): 1401507, https://doi.org/10.1002/aenm.201401507.

30. L. N. Skov, J. B. Grinderslev, and T. R. Jensen, "Layered Titanium Sulfide Cathode for all-Solid-State Magnesium Batteries," *Batteries & Supercaps* 6 (2023): 202300185.

31. A. S. Bandarenka, "Exploring the Interfaces Between Metal Electrodes and Aqueous Electrolytes With Electrochemical Impedance Spectroscopy," *The Analyst* 138 (2013): 5540–5554, https://doi.org/10.1039/c3an00791j.

32. W. Wang, X. Wei, D. Choi, X. Lu, and G. Yang, *Sun in Advances in Batteries for Medium and Large-Scale Energy Storage*, (Elsevier, 2015): pp. 3–28.

33. M. Vyas, K. Pareek, S. Sapre, and A. Garg, "Single point diagnosis of short circuit abuse condition in lithium-ion battery Through impedance data," *International Journal of Energy Research* 45 (2021): 18212–18221, https://doi.org/10.1002/er.6972.

34. S. Menkin, J. B. Fritzke, R. Larner, et al., "Insights Into Soft Short Circuit-based Degradation of Lithium Metal Batteries," *Faraday Discussions* 248 (2024): 277–297.

35. S. Tan, J. Xu, R. Deng, et al., "A Perspective on the Key Factors of Safety for Rechargeable Magnesium Batteries," *Journal of Energy Chemistry* 94 (2024): 656–676, https://doi.org/10.1016/j.jechem.2024.03.015.

36. Z. Li, X. Mu, Z. Zhao-Karger, et al., "Fast Kinetics of Multivalent Intercalation Chemistry Enabled by Solvated Magnesium-ions Into Self-established Metallic Layered Materials," *Nature Communications* 9 (2018): 5115, https://doi.org/10.1038/s41467-018-07484-4.

37. M. Sadd, S. Xiong, J. R. Bowen, F. Marone, and A. Matic, "Investigating Microstructure Evolution of Lithium Metal During Plating and Stripping via Operando X-ray Tomographic Microscopy," *Nature Communications* 14 (2023): 854, https://doi.org/10.1038/s41467-023-36568-z.

38. X. Guan, A. Wang, S. Liu, et al., "Controlling Nucleation in Lithium Metal Anodes," *Small* 14 (2018): 1801423.

39. F. Shi, A. Pei, A. Vailionis, et al., "Strong Texturing of Lithium Metal in Batteries," *Proceedings of the National Academy of Sciences* 114 (2017): 12138–12143, https://doi.org/10.1073/pnas.1708224114.

40. S.-Y. Ha, Y.-W. Lee, S. W. Woo, et al., "Magnesium(II) Bis(trifluoromethane sulfonyl) Imide-Based Electrolytes With Wide Electrochemical Windows for Rechargeable Magnesium Batteries," *ACS Applied Materials & Interfaces* 6 (2014): 4063–4073, https://doi.org/10.1021/am405619v.

41. O. W. Elkhafif, H. K. Hassan, M. Hashmi, N. Arya, M. Anjass, and T. Jacob, "Boosting Mg Deposition and Dissolution From Ionic Liquids—The Role of Different Additives for Applications in Mg-ion Batteries," *Journal of Energy Storage* 105 (2025): 114636, https://doi.org/10.1016/j.est.2024.114636.

16146840, 0, Downloaded from https://advanced.onlinelibrary.wiley.com/doi/10.1002/aenm.202505315 by Karlsruher Institut Für Technologie, Wiley Online Library on [04/12/2025]. See the Terms and Conditions (https://onlinelibrary.wiley.com/terms-and-conditions) on Wiley Online Library for rules of use; OA articles are governed by the applicable Creative Commons License

42. R. Davidson, A. Verma, D. Santos, et al., "Mapping Mechanisms and Growth Regimes of Magnesium Electrodeposition at High Current Densities," *Materials Horizons* 7 (2020): 843–854, https://doi.org/10.1039/C9MH01367A.

43. M. Jäckle, K. Helmbrecht, M. Smits, D. Stottmeister, and A. Groß, "Self-diffusion Barriers: Possible Descriptors for Dendrite Growth in Batteries?," *Energy & Environmental Science* 11 (2018): 3400–3407, https://doi.org/10.1039/C8EE01448E.

44. P. Hundekar, S. Basu, X. Fan, et al., "In Situ Healing of Dendrites in a Potassium Metal Battery," *Proceedings of the National Academy of Sciences* 117 (2020): 5588–5594, https://doi.org/10.1073/pnas.1915470117.

45. P. Hundekar, S. Basu, J. Pan, et al., "Exploiting Self-heat in a Lithium Metal Battery for Dendrite Healing," *Energy Storage Materials* 20 (2019): 291–298, https://doi.org/10.1016/j.ensm.2019.04.013.

46. J. Eaves-Rathert, K. Moyer, M. Zohair, and C. L. Pint, "Kinetic- versus Diffusion-Driven Three-Dimensional Growth in Magnesium Metal Battery Anodes," *Joule* 4 (2020): 1324–1336, https://doi.org/10.1016/j.joule.2020.05.007.

47. F. Fiesinger, D. Gaissmaier, M. van den Borg, and T. Jacob, "First-Principles Studies on the Atomistic Properties of Metallic Magnesium as Anode Material in Magnesium-Ion Batteries," *ChemSusChem* 15 (2022): 202200414, https://doi.org/10.1002/cssc.202200414.

48. T. Yang, J. Liu, J. Dai, and Y. Han, "Shaping Particles by Chemical Diffusion and Reaction," *CrystEngComm* 19 (2017): 72–79, https://doi.org/10.1039/C6CE02068B.

49. H. Wang, Y. Han, and J. Li, "Dominant Role of Compromise Between Diffusion and Reaction in the Formation of Snow-Shaped Vaterite," *Crystal Growth & Design* 13 (2013): 1820–1825, https://doi.org/10.1021/cg301241s.

50. Y. Zuo, K. Wang, P. Pei, et al., "Zinc Dendrite Growth and Inhibition Strategies," *Materials Today Energy* 20 (2021): 100692, https://doi.org/10.1016/j.mtener.2021.100692.

51. P. Canepa, G. S. Gautam, R. Malik, et al., "Understanding the Initial Stages of Reversible Mg Deposition and Stripping in Inorganic Nonaqueous Electrolytes," *Chemistry of Materials* 27 (2015): 3317–3325, https://doi.org/10.1021/acs.chemmater.5b00389.

52. I. Weber, J. Ingenmey, J. Schnaidt, B. Kirchner, and R. J. Behm, "Influence of Complexing Additives on the Reversible Deposition/Dissolution of Magnesium in an Ionic Liquid," *ChemElectroChem* 8 (2021): 390–402, https://doi.org/10.1002/celc.202001488.

53. Y. Lu, C.-Z. Zhao, H. Yuan, X.-B. Cheng, J.-Q. Huang, and Q. Zhang, "Critical Current Density in Solid-State Lithium Metal Batteries: Mechanism, Influences, and Strategies," *Advanced Functional Materials* 31 (2021): 2009925, https://doi.org/10.1002/adfm.202009925.

54. A. Morag, X. Chu, C. Neumann, et al., "Ionic Liquid Electrolyte Additive Regulates the Multi-species-insertion Titanium Sulfide Cathode for Magnesium Batteries," *Energy Storage Materials* 53 (2022): 435–443, https://doi.org/10.1016/j.ensm.2022.09.021.

55. F. Chu, J. Hu, J. Tian, X. Zhou, Z. Li, and C. Li, "Situ Plating of Porous Mg Network Layer to Reinforce Anode Dendrite Suppression in Li-Metal Batteries," *ACS Applied Materials & Interfaces* 10 (2018): 12678–12689.

56. S. Eom, M. Park, B. Koo, et al., "Suppressing Organic Cation Reactivity in Locally Concentrated Ionic Liquid Electrolytes for Lithium Metal Batteries," *Energy Storage Materials* 74 (2025): 103966, https://doi.org/10.1016/j.ensm.2024.103966.

57. T. Torimoto, T. Tsuda, K. Okazaki, and S. Kuwabata, "New Frontiers in Materials Science Opened by Ionic Liquids" *Advanced Materials* 2010, 22, 1196–1221.

58. H. Wang, X. Feng, Y. Chen, et al., "Reversible Electrochemical Interface of Mg Metal and Conventional Electrolyte Enabled by Intermediate Adsorption," *ACS Energy Letters* 5 (2020): 200–206, https://doi.org/10.1021/acsenergylett.9b02211.

59. J. Z. Hu, N. N. Rajput, C. Wan, et al., "25Mg NMR and Computational Modeling Studies of the Solvation Structures and Molecular Dynamics in Magnesium Based Liquid Electrolytes," *Nano Energy* 46 (2018): 436–446, https://doi.org/10.1016/j.nanoen.2018.01.051.

60. D. Zhang, Y. Sun, X. Liu, et al., "Borohydride-Based Interphase Enabling Reversible Magnesium Metal Anode in Conventional Electrolytes," *ACS Energy Letters* 9 (2024): 2685–2695, https://doi.org/10.1021/acsenergylett.4c00757.

61. L. Li, S. Basu, Y. Wang, et al., "Self-heating–induced Healing of Lithium Dendrites," *Science* 359 (2018): 1513–1516, https://doi.org/10.1126/science.aap8787.

62. Y. Zhang, Y. Li, W. Shen, K. Li, and Y. Lin, "Important Role of Atom Diffusion in Dendrite Growth and the Thermal Self-Healing Mechanism," *ACS Applied Energy Materials* 6 (2023): 1933–1945, https://doi.org/10.1021/acsaem.2c03864.

Supporting Information

Additional supporting information can be found online in the Supporting Information section.

Supporting file: aenm70465-sup-0001-SuppMat.docx **Supporting file**: aenm70465-sup-0002-MovieS1.mp4 **Supporting file**: aenm70465-sup-0003-MovieS2.mp4 **Supporting file**: aenm70465-sup-0004-MovieS3.mp4 **Supporting file**: aenm70465-sup-0005-MovieS4.mp4

16146840, 0, Downloaded from https://advanced.onlinelibrary.wiley.com/doi/10.1002/aenm.202505315 by Karlsruher Institut Für Technologie, Wiley Online Library on [04/12/2025]. See the Terms and Conditions (https://onlinelibrary.wiley.com/terms-and-conditions) on Wiley Online Library for rules of use; OA articles are governed by the applicable Creative Commons License